Interplay between breathing-mode distortions and magnetic order in rare-earth nickelates from *ab initio* magnetic models

Danis I. Badrtdinov, Alexander Hampel, and Cyrus E. Dreyer

Phys. Rev. B **104**, 054403 — Published 3 August 2021

DOI: 10.1103/PhysRevB.104.054403

Interplay between breathing-mode distortions and magnetic order in rare-earth nickelates from *ab initio* magnetic models

Danis I. Badrtdinov,[1,2] Alexander Hampel,[2,*] and Cyrus E. Dreyer[2,3]

[1] *Theoretical Physics and Applied Mathematics Department, Ural Federal University, 620002 Yekaterinburg, Russia*

[2] *Center for Computational Quantum Physics, Flatiron Institute, 162 Fifth avenue, New York, NY 10010, USA*

[3] *Department of Physics and Astronomy, Stony Brook University, Stony Brook, New York, 11794-3800, USA*

(Dated: June 15, 2021)

We use density-functional theory calculations to explore the magnetic properties of perovskite rare-earth nickelates, $\mathcal{R}NiO_3$, by constructing microscopic magnetic models containing all relevant exchange interactions via Wannierization and Green's function techniques. These models elucidate the mechanism behind the formation of antiferromagnetic order with the experimentally observed propagation vector, and explain the reason previous DFT plus Hubbard U calculations favored ferromagnetic order. We perform calculations of magnetic moments and exchange-coupling parameters for different amplitudes of the R_1^+ breathing mode distortion, which results in expanded and compressed NiO_6 octahedra. Our analysis shows that the strong competition between nearest neighbor ferromagnetic and next-nearest neighbor antiferromagnetic couplings determine the magnetic ordering. The inclusion of spin-orbit coupling demonstrates that the magnetic anisotropy is very small, while the magnetic moments of the short bond nickel atoms tend to zero similar to the collinear case. Finally, we show that nickelates with larger rare-earth ions display overall stronger exchange couplings, resulting in a more stable antiferromagnetic phase. Our results provide a clear picture of the trends of the magnetic order across the nickelate series and give insights into the coupling between magnetic order and structural distortions.

I. INTRODUCTION

Rare-earth (RE) nickelate perovskites, with the chemical formula $\mathcal{R}NiO_3$, have received significant attention due to their rich phase diagram. As a function of the ionic size of RE element $\mathcal{R}$[1–4], a combined structural and metal-insulator transition (MIT) occurs with temperature, as well as the formation of long-range magnetic order. Both can be tuned by external pressure[5], strain[6] and reduced dimensionality[7]. This tunability paves the way for engineering nanoelectronic and spintronic devices[8–10].

The structural transition, which occurs in all RE nickelates except $LaNiO_3$, is characterized by a symmetry lowering from the orthorhombic $Pbnm$ to the monoclinic $P2_1/n$ spacegroup upon cooling; it can be described mainly by a "breathing-mode" distortion, which creates expanded and compressed NiO_6 octahedra arranged in a three dimensional checkerboard pattern. We refer to the two different Ni sites that result as residing in either the long bond (LB) or short bond (SB) octahedra[11] (Fig. 1).

This distortion strongly modifies the electronic configuration and the corresponding magnetic moments of the Ni atoms. One of the proposed descriptions of the resulting electronic structure[12] suggests that the initial electronic configuration of the Ni atoms, i.e., $3d^7$ with spin $S = \frac{1}{2}$, transforms to two charge-disproportionated Ni sublattices $3d^6$ ($S = 0$) and $3d^8$ ($S = 1$) under the distortion. However, this atomic picture does not consider the strong hybridization between Ni-$3d$ and O-$2p$ orbitals. Hence, later studies introduced a more complete description of the electronic configuration including oxygen (ligand) "holes," denoted as $\underline{L}$[13,14], and describing the connected structural-MIT in nickelates as a site-selective Mott transition[13,15–19]. The resulting SB and LB octahedra are described by $d^8\underline{L}^0$ and $d^8\underline{L}^2$ states with total spins tending toward $S = 0$ and $S = 1$, respectively. Conventional density functional theory (DFT) based methods also support this interpretation, showing different magnetic moments of Ni_{SB} and Ni_{LB} atoms, while demonstrating nearly equal integrated charges around both Ni atoms inside the projector augmented wave (PAW) spheres[1,15]. However, such an analysis will depend on the size of the augmentation region[20], and cannot fully capture the hybridization with the oxygens; a more complete picture may be obtained, e.g., via constructing Wannier functions for the (possibly hybridized) Ni $3d$ states[2].

At low temperatures, RE nickelates (again with the exception of $LaNiO_3$) exhibit an antiferromagnetic (AFM) insulating ground state. The magnetic structure has a propagation vector of $\mathbf{q} = (\frac{1}{4}, \frac{1}{4}, \frac{1}{4})$ (in pseudocubic notation), which was probed by neutron scattering for bulk systems[11,21–24] and resonant soft X-ray scattering (RIXS) for thin film heterostructures[25,26]. The exact arrangement of magnetic moments in the systems is still under debate and strongly depends on the interpretation of experimental data[3,18]. Particularly, neutron data suggests a collinear magnetic ordering, where the magnetic moment of SB nickel atoms vanish[18,23,24]. One candidate for the ground-state magnetic configuration is a T-type AFM (T-AFM) structure[1,3], depicted in Fig. 2(a). In this structure, the LB moments are arranged in an "up-up-down-down" ($\uparrow\uparrow\downarrow\downarrow$) pattern in all three Cartesian directions, and the SB moments tend to zero with increasing R_1^+ amplitude.

On the other hand, the corresponding RIXS spectra

have been interpreted as a non-collinear (NCL) arrangement of spins with clearly non-zero SB magnetic moments[25–27], also involving the ↑↑↓↓ pattern in all three Cartesian directions [see Fig. 2(b)]. Here, all moments lie in the *ac* plane, with their direction reversed upon moving along [1, 0, 1]. This magnetic configuration can be considered as an orthogonal spin spiral. More importantly, the nearest neighbor SB and LB magnetic moments are perpendicular to each other, which can weaken interactions between them.

There have been many studies based on DFT, including with hybrid functionals[28], DFT+U[1,2,29–32], and DFT+DMFT[15,17–19,33] aimed at addressing the discrepancy in the experimentally-determined magnetic orderings. One key challenge is that the *ferromagnetic* ordering is often predicted by DFT+U to be the most energetically favorable, though is not observed experimentally, in contrast to the main candidates for the ground state: the collinear T-AFM and NCL order [Fig. 2(a) and (b)]. Also, there exist several other AFM orderings that have been proposed, but they either are not compatible with the experimental order vector (e.g., E-AFM) or have been shown to be energetically very similar to T-AFM (e.g., S-AFM, N-AFM)[1,2,29].

The goal of this work is to elucidate the *microscopic* mechanisms in the RE nickelates that drive their magnetic properties, and influence the magnetic orderings predicted by DFT-based calculations. To this end, spin models are constructed for a series of RE nickelates: $PrNiO_3$, $SmNiO_3$ and $LuNiO_3$, by obtaining Wannier functions for the hybridized Ni($3d$)-O($2p$) orbitals, and then using the local force theorem approach[34,35] to extract exchange couplings. We analyze the evolution of the magnetic interactions under the R_1^+ structural breathing mode distortion, and across the series. Calculations are based on DFT plus Hubbard U (DFT+U), but we do not limit ourselves to the ground-state magnetic ordering. Instead, we utilize calculations performed with FM, collinear T-AFM, and noncolinar (NCL) orderings to demonstrate the microscopic driving forces for the magnetic ordering. Our calculations reveal strong ferromagnetic nearest-neighbor and weaker antiferromagnetic next-nearest-neighbor couplings, which are induced due to magnetically active Ni d_{z^2} and $d_{x^2-y^2}$ states. Competition between these couplings plays the dominant role in determining the formation of magnetic order in $\mathcal{R}NiO_3$ systems and explains why previous theoretical calculations favored ferromagnetic ordering. The inclusion of spin-orbit coupling demonstrates that the magnetic anisotropy is very small, while the magnetic moments of SB nickel atoms tend to zero for finite R_1^+ amplitude even in the NCL case.

The remainder of this paper is organized as follows. Sec. II covers the methods and theories used in our calculations. In Sec. III, we present our main results for magnetic moments and interactions of selected rare-earth nickelate systems: $PrNiO_3$, $SmNiO_3$ and $LuNiO_3$. We discuss the implications of our results on the proposed magnetic structures in Sec. IV. Finally, Sec. V concludes the paper.

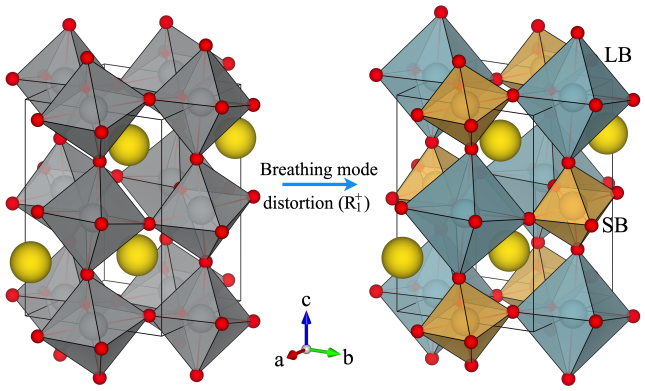

FIG. 1. Evolution of the crystal structure of $\mathcal{R}NiO_3$ under the breathing mode distortion R_1^+, which leads to formation of short bond (SB) and long bond (LB) NiO_6 octahedra. The rare-earth element $\mathcal{R}$ is denoted by yellow spheres. Crystal structures are visualized using the VESTA software[36].

II. THEORETICAL FRAMEWORK

A. Formalism

We construct the following spin model, which describes the energetics of individual spins $\mathbf{S}_i$ on nickel atoms interacting via isotropic exchange couplings J_{ij}:

$$\hat{\mathcal{H}}^{\text{spin}} = \sum_{i>j} J_{ij} \hat{\mathbf{S}}_i \hat{\mathbf{S}}_j. \tag{1}$$

The exchange integrals can be calculated using the local force theorem approach[34,35]

$$J_{ij} = \frac{1}{2\pi S^2} \sum_{m,m',n,n'} \times \\ \text{Im} \int_{-\infty}^{E_F} d\epsilon \left[\Delta_i^{mm'} G_{ij\downarrow}^{m'n}(\epsilon) \Delta_j^{nn'} G_{ji\uparrow}^{n'm}(\epsilon) \right], \tag{2}$$

where m, m', n, n' are orbital indices running over Ni $3d$ ($l = 2$) states, E_F is the Fermi energy, $S = \frac{1}{2}$ is the spin quantum number[37], $\Delta_i^{mm'} = H_{ii\uparrow}^{mm'} - H_{ii\downarrow}^{mm'}$ is the on-site potential, and G is the single-particle Green's functions

$$G_{ij\sigma}^{mn'}(\epsilon) = \frac{1}{N_{\mathbf{k}}} \sum_{\mathbf{k},l}^{M} \frac{c_{i\sigma}^{nl}(\mathbf{k}) c_{j\sigma}^{n'l^*}(\mathbf{k})}{\epsilon - E_\sigma^l(\mathbf{k})}. \tag{3}$$

Here $N_{\mathbf{k}}$ is the number of k points in the first Brillouin zone (BZ), $c_{i\sigma}^{nl}(\mathbf{k})$ stands for the component of lth eigenstate in the basis of Wannier functions, with eigenvalue $E_\sigma^l(\mathbf{k})$. The summation in Eq. (3) runs over all Ni($3d$)

and O(2p) orbitals; since n and n' only consist of Ni(3d) orbitals, this corresponds to projecting the Wannier functions onto Ni(3d) states, thus capturing the overlap between Ni(3d) and O(2p).

The magnetic moment of a selected nickel site can also be evaluated as

$$m_i = -\frac{1}{\pi}\mathrm{Im}\int_{-\infty}^{E_F} d\epsilon\, \mathrm{Tr}_n\left[G^{nn}_{ii\uparrow}(\epsilon) - G^{nn}_{ii\downarrow}(\epsilon)\right]. \quad (4)$$

Eq. (4) includes in the Ni moments the contribution from the overlap with oxygen. If we define a different set of Green's functions by allowing n and n' in Eq. (3) to run over all of the Wannier functions (not just nickel 3d), then Eq. (4) corresponds to the total magnetic moment per site, equivalent to integrating over the density of states near the Fermi level; by limiting the trace over just the Ni(3d) or just O(2p) Wannier functions, we can obtain separate moments on the nickels and oxygens, which may be compared to those integrated within the PAW spheres[20], as discussed in the next section.

B. Computational approach

We calculated the exchange couplings in Eq. (2) using DFT with the generalized-gradient approximation exchange-correlation functional of Perdew, Burke, and Ernzerhof[38] and the projector augmented wave (PAW) method[39] as implemented in the Vienna *ab-initio* Simulation Package (`VASP`)[40,41]. For the rare-earth atoms, we used PAW potentials corresponding to a 3+ valence state with f-electrons frozen into the core; for Ni, the 3p semi-core states were included as valence electrons. We set the energy cutoff of the plane-wave basis to 550 eV and the energy convergence criteria to 10^{-8} eV.

Correlation effects were taken into account on the static mean-field level using the DFT+U method[42], where we considered an effective on-site Coulomb U and Hund's exchange J_H interactions in the rotationally invariant form[43]. A value of $J_H = 1$ eV can be used for compounds with 3d orbitals[44,45], while the on-site Coulomb parameter depends on the specific system. Previous results showed that the best agreement with experiment can be obtained using a relatively small value of $U = 2$ eV. Using such a small U ensures that the AFM magnetic state is lower in energy than the FM state for $\mathcal{R}$ =Pr, and $\mathcal{R}$ =Sm[1,2,32]. Therefore, we used $U = 2$ eV and $J_\mathrm{H} = 1$ eV for the majority of our DFT+U calculations, and comment on how a larger U ($U = 5$ eV) may effect the results.

From the calculated electronic structure, maximally-localized Wannier functions[46] were generated using the `wannier90` package[47]. We constructed Wannier functions for all occupied and unoccupied Ni 3d and O 2p states. This ensures that the obtained Wannier functions for both spin channels are well localized (Fig. 3), and we can use them as an atomic-like basis for Eqs. (2) and (3). Note, that this choice is different to Ref. 2, were Wannier functions were only constructed for the occupied states. Since the f electrons of the RE elements are frozen into core states, we neglected their magnetic ordering, which only occurs at very low temperatures[23,24].

To examine different magnetic orders we considered two types of cells: the primitive monoclinic cell containing 20 atoms, and a cell enlarged in the a and c directions containing 80 atoms (necessary for the AFM orderings); an 8×8×6 and 4×6×4 Monkhorst-Pack mesh for the Brillouin-zone integration was used for the 20 and 80 atom cells, respectively. The number of k-points within the first Brillouin zone for the evaluation of the Green's function [Eq. (3)] and energy points for integration over a semicircular contour in the upper half of the complex energy plane [Eqs. (2) and (4)] were chosen to reach numerical convergence of the exchange couplings within 0.1 meV.

For a systematic study of structural distortion, we used a symmetry-based mode decomposition analysis[48] where we varied the amplitude of specific modes expressed in terms of irreducible representations of the parent (cubic perovskite) $Pm\bar{3}m$ structure. The most significant modes that are present in the RE nickelates include octahedral rotation modes M_3^+ (in-phase) and R_4^+ (out-of-phase), and the breathing mode distortion R_1^+[49]. The breathing mode, which is responsible for the formation of SB and LB octahedral (Fig. 1), is the distortion most strongly coupled to the magnetic structure, so it will be the focus of this study. The main effect of the different RE atoms is to change the amplitude of the octahedral rotation modes. Specifically, smaller radii REs correspond to larger rotations. Thus the range in RE atoms in this study demonstrates the influence of octahedral rotations on the magnetic ordering.[33].

In our calculations, we start from the high-temperature orthorhombic $Pbnm$ structure, relaxed with non-magnetic DFT (with $U = 0$)[1]; in this case, SB and LB octahedra have the same volume. We then gradually increase the R_1^+ amplitude, calculating how the exchange couplings and magnetic moments are modified by the distortion. Thus we can study the evolution of magnetic characteristics with the transition from $Pbnm$ to the low temperature insulating monoclinic phase $P2_1/n$.

III. RESULTS

A. Magnetic moment analysis

We begin with the magnetic moments of $PrNiO_3$, $SmNiO_3$ and $LuNiO_3$, assuming FM or T-AFM ordering, using the on-site Green's functions [Eq. (4)] in the Wannier basis. This procedure will correctly capture the hybridization effect between nickel and oxygen states and the corresponding distribution of magnetic moment density[2].

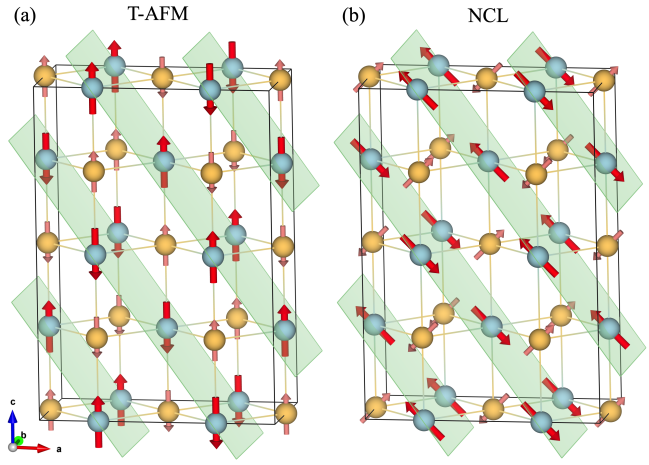

FIG. 2. (a) T-type antiferromagnetic (AFM) and (b) non-colinear (NCL) magnetic configurations as a possible ground state magnetic orderings in $\mathcal{R}NiO_3$ with experimental propagation vector $\mathbf{q} = (\frac{1}{4}, \frac{1}{4}, \frac{1}{4})$. Yellow and blue spheres correspond to Ni_{SB} and Ni_{LB} atoms respectively, which have smaller and larger magnetic moments corresponding to the length of the red arrows.

Nickel magnetic moments versus R_1^+ amplitude are shown in Fig. 4(a)-(c). Dashed vertical lines denote the experimental breathing-mode amplitudes for $PrNiO_3$ (0.045 Å[50]) and $LuNiO_3$ (0.075 Å[51]), and the theoretically predicted amplitude for $SmNiO_3$ (0.060 Å[33]), where no experimental data on the low temperature phase is available. In the case of the high-temperature orthorhombic phase ($R_1^+ = 0$ Å), in which all Ni octahedra have the same volume, FM order leads to magnetic moments of $\simeq 0.9\,\mu_B$ per nickel atom for all materials. Within the T-AFM order the *Pbnm* symmetry is broken, causing a small variation of magnetic moments for the inequivalent Ni sites. The difference between the SB and LB moments strongly increases with larger R_1^+ breathing mode amplitudes. In the FM case, the SB Ni magnetic moment smoothly decreases; for T-AFM, the moment quickly vanishes at a modest value of R_1^+. The amplitude where the SB moment goes to zero depends on the rare-earth element, specifically it is larger for $LuNiO_3$ than $PrNiO_3$ and $SmNiO_3$. In all cases, the R_1^+ amplitudes at which the SB moment vanish are much smaller than the experimentally observed amplitudes for these compounds. Therefore, DFT+U predicts $m_{SB} = 0$ for T-AFM order for all experimental structures. In contrast, m_{LB} increases with R_1^+ and converges to $\simeq 1.3\,\mu_B$ for both FM and T-AFM order. The obtained values of the LB nickel magnetic moment are in good agreement with experimental findings, which report values in the range $1 - 1.8\,\mu_B$[3,18,22–24,27,51–53].

The Wannier-based analysis allows us to analyze the orbital contributions to total nickel magnetic moments, and we find that for both FM and T-AFM order, LB and SB moments originate almost entirely from Ni e_g states. Since the corresponding Ni t_{2g} states are fully occupied, they are not magnetically active.

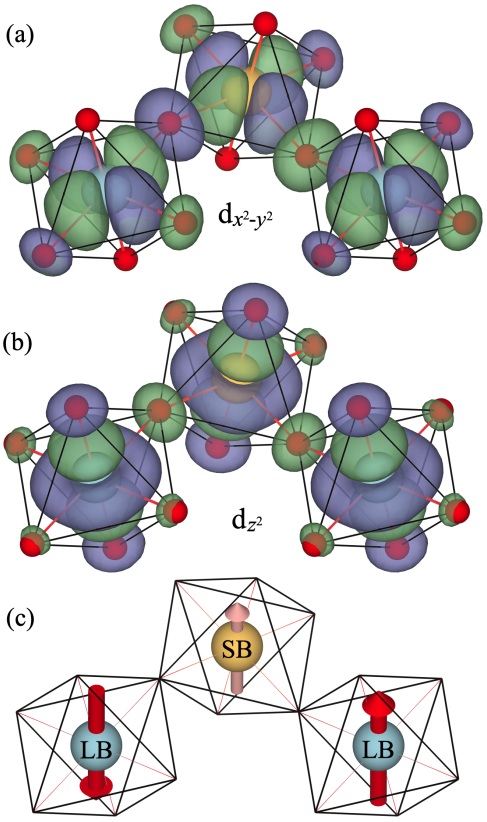

FIG. 3. Maximally localized Wannier functions of the long-bond (LB) and short-bond (SB) nickel atoms. (a) corresponds to $d_{x^2-y^2}$ and (b) to d_{z^2} orbitals for nearest neighbor LB – SB – LB nickel atoms, calculated for the T-AFM $PrNiO_3$ system at the experimental breathing mode amplitude $R_1^+ =$ 0.045 Å. Only spin majority orbitals at each nickel atoms are represented for clarity, spin moments are shown in (c).

These obtained results are consistent with the picture that would emerge from an analysis of the magnetization within the PAW spheres around Ni and O. The nickel moment from the Wannier analysis (and its dependence on R_1^+) is in good agreement ($\sim 0.01\,\mu_B$) with the moments in Ni PAW spheres. This indicates that the magnetism is localized around the atoms, instead of in the interstitial regions[54]. Similarly to the PAW estimation, the Wannier based oxygen magnetic moments for all magnetic configurations are very small (less than 0.05 μ_B). This suggests that, while there is significant Ni-O hybridization, the moment resides only at the Ni sites.

The magnitude of the magnetic moments depends on the choice of U parameter of DFT+U. Increasing U leads to a stronger localization of the $3d$ electrons, and consequently gives comparably larger total magnetic moments of nickel atoms. The reason for this can be seen in the density of states, e.g., for $PrNiO_3$ (Fig. 5), where a larger U value leads to stronger splitting between spin channels of LB nickel e_g states, enhancing their magnetic moment.

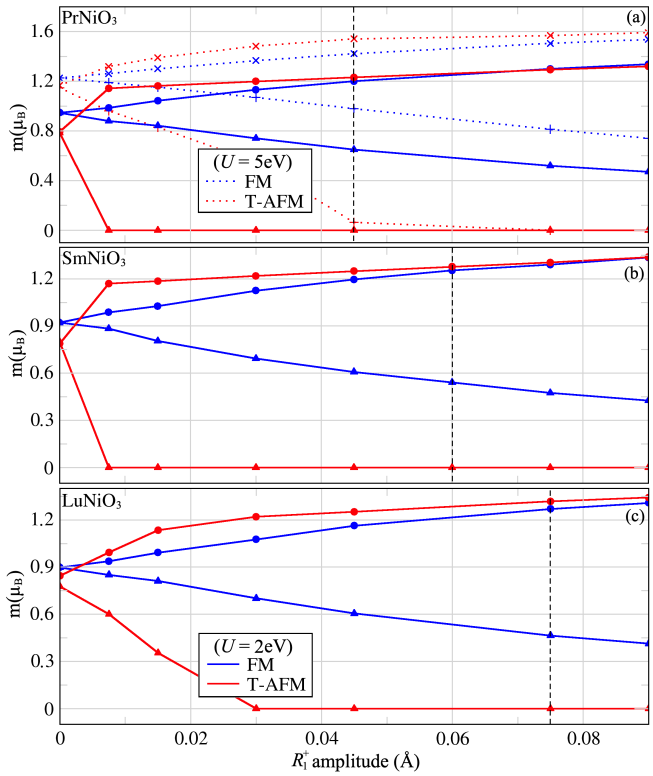

FIG. 4. LB (circles) and SB (triangles) magnetic moments of (a) $PrNiO_3$, (b) $SmNiO_3$, and (c) $LuNiO_3$ as a function of the R_1^+ amplitude, calculated for different magnetic states using $U = 2$ eV. Dashed vertical lines correspond to experimentally observed breathing mode amplitudes from Ref. 50 for $PrNiO_3$ and Ref. 51 for $LuNiO_3$, and the theoretically predicted amplitude for $SmNiO_3$ from Ref. 33. The $R_1^+ = 0$ structure corresponds to the high temperature orthorhombic *Pbnm* structure. The dotted curves (LB (crosses) and SB (pluses)) for $PrNiO_3$ represent results obtained with $U = 5$ eV.

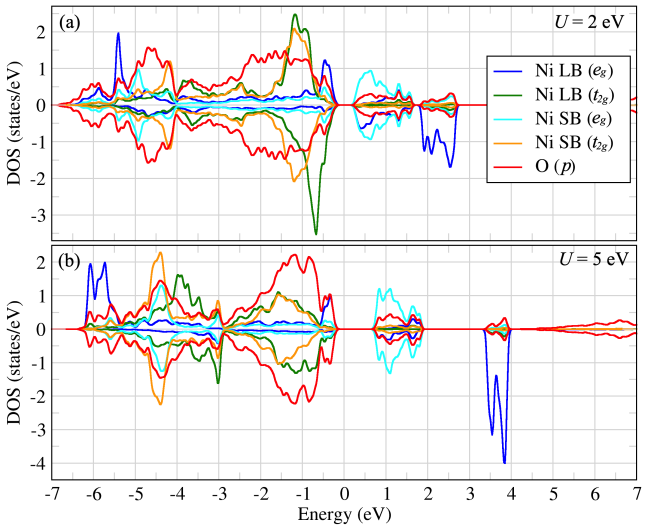

FIG. 5. Partial densities of states (DOS) using the PAW projectors for $PrNiO_3$ at the experimental $R_1^+ = 0.045$ Å amplitude, calculated with T-AFM order for (a) $U = 2$ eV and (b) $U = 5$ eV. Here, only t_{2g} and e_g states contributions of a single LB and SB nickel atom, as well as $2p$ states of the surrounding six oxygen atoms in NiO_6 octahedra are shown. The different occupation of the e_g spin channels of the LB nickel reflect the magnetic moment, while for SB both spin channels are equally occupied, leading to a zero moment.

To demonstrate this effect, we show magnetic moments calculated using $U = 5$ eV for $PrNiO_3$ [see Fig. 4(a)]. The resulting magnetic moments for *Pbnm* are larger than those obtained with $U = 2$ eV. For instance, the large R_1^+ amplitude LB moments (for both magnetic orders) converge to $\simeq 1.3\,\mu_B$ for $U = 2$ eV versus $\simeq 1.5\,\mu_B$ for $U = 5$ eV. Furthermore, $m_{\rm SB}$ for T-AFM order becomes zero at comparably larger value $R_1^+ \simeq 0.05$ Å compared to ≤ 0.007 Å for $U = 2$ eV, as was found in previous DFT+U studies[1].

B. Exchange couplings

We now perform a quantitative analysis of the various magnetic interactions present in the $\mathcal{R}NiO_3$ materials with respect to R_1^+ amplitude. In Fig. 6 we show a schematic of the exchange interactions included in our study. The LB and SB Ni sublattices are depicted as blue and yellow spheres, and the RE and oxygens are removed for clarity. Focusing on a LB site, there are two inequivalent nearest-neighbor interactions with SB sites in the *ab* plane (J_1). Also in the *ab* plane, we consider next-nearest-neighbor interactions with other LB sites J_2 and J_3, as well as next-next-nearest neighbor interactions J_4. In the *c* direction, we have nearest neighbor interactions between LB and SB sites (J_5), and next-nearest neighbor (J_7 and J_6) interactions.

1. *Ferromagnetic interactions J_1 and J_5*

The calculated magnetic interactions via Eq. (2) depend on the reference magnetic configuration used in the underlying DFT calculation[55], since the electronic structure and the resulting single-particle Green's functions will be different for FM and T-AFM order. Since the T-AFM order leads to a suppression of the SB magnetic moment (Fig. 4) the nearest-neighbor exchange interactions J_1 and J_5 are suppressed, as they couple two different types of nickel sites in the *ab* plane and along the *c* direction (Fig. 6). Therefore, for these interactions we focus on the FM state as the reference magnetic order. Resulting values as a function of R_1^+ are given in Fig. 7.

In general, short range interactions originate from a combination of different mechanisms[44,45]. Previous studies reported that the charge fluctuation between SB Ni and LB Ni sites with unequal spins will lead to ferromag-

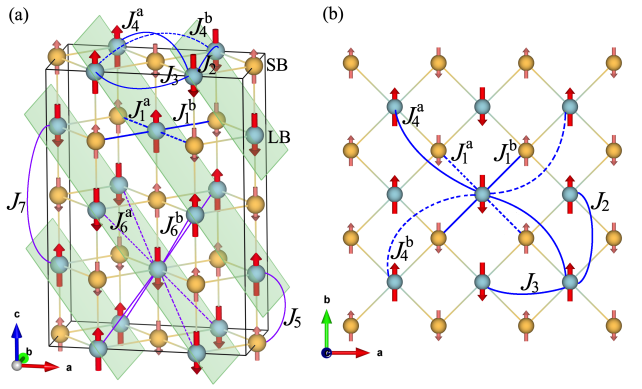

FIG. 6. Magnetic model of $\mathcal{R}NiO_3$ system with main exchange interactions plotted in (a) side and (b) top view. Blue and yellow spheres correspond to Ni in long bond (LB) and short bond (SB) octahedra, respectively. All other atoms are removed for clarity. Arrows represent magnetic moments of nickel atoms in the T-AFM order. Corresponding interactions between SB nickels are also included, but not shown in the figure for clarity.

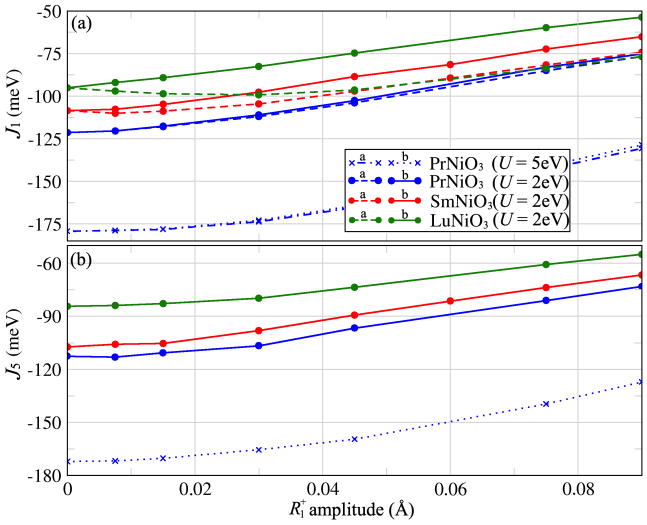

FIG. 7. Nearest neighbor (a) $J_1^{a/b}$ and (b) J_5 exchange couplings (see Fig. 6) between nickel atoms in $\mathcal{R}NiO_3$ as a function of breathing mode distortion R_1^+ amplitude. The reference magnetic configuration is FM. The additional dotted curves for $PrNiO_3$ denoted by crosses represent results obtained with $U = 5$ eV.

netic double exchange $J^{\rm DE} < 0$ process, which competes with the conventional antiferromagnetic superexchange $J^{\rm SE} > 0$[26,27]. The resulting coupling $J = J^{\rm SE} + J^{\rm DE}$ can have either sign depending on which mechanism will prevail. We show in Fig. 7 strong FM interaction (i.e., negative values) for both J_1 and J_5, implying $|J^{\rm SE}| < |J^{\rm DE}|$ for both cases. Double exchange between the Ni atoms requires inequivalent charges on the sites[56,57]. The strength of double exchange, and thus the FM couplings, would be expected to increase with R_1^+[26]. However, in our calculations the magnitude of J_1 and J_5 couplings gradually *decrease* with increasing R_1^+ amplitudes. This suggests that other factors (e.g., charge transfer to oxygen states) are important in the resulting exchange interactions.

As a result of the presence of M_3^+ and R_4^+ rotation modes, the nearest neighbor exchange J_1 splits into two groups J_1^a and J_1^b for finite R_1^+ (Fig. 6). The value of this splitting depends on the rare-earth element $\mathcal{R}$ (c.f., solid and dashed curves in Fig. 7). In particular, a stronger splitting $J_1^a < J_1^b$ can be found for $LuNiO_3$ compared to $PrNiO_3$, where $J_1^a \simeq J_1^b$. Hence, this magnitude of the splitting is connected to the magnitude of the octahedral rotation modes M_3^+ and R_4^+[1]. As mentioned in Sec. II B, RE elements with smaller effective radii will cause stronger M_3^+ and R_4^+ rotations of NiO_6 octahedra, modifying Ni – O – Ni angles, and resulting in a larger difference between J_1^a and J_1^b.

Furthermore, higher U parameters will lead to a stronger localization of d electrons, which influences not only the magnetic moments (Fig. 4), but also the corresponding exchange interactions between them. Our calculations on $PrNiO_3$ with $U = 5$ eV show an enhancement of the nearest neighbor ferromagnetic J_1 and J_5 couplings (Fig. 7). This is directly related to the fact that using a larger on-site Coulomb interaction parameter will decrease the AFM superexchange term, which is inversely proportional to U. Double exchange is proportional to the transfer integral between Ni site, and does not depend directly on U[57].

2. *Antiferromagnetic interactions J_4 and J_7*

Next-nearest-neighbor exchange interactions J_4 and J_7 connect the same type (SB or LB) of nickel atom (Fig. 6). Similar to the nearest-neighbor J_1 interaction, the next nearest neighbor J_4 also splits into two groups J_4^a and J_4^b. The value of this splitting depends on the RE element via the octahedral rotation modes M_3^+ and R_4^+. These interactions are antiferromagnetic, i.e., positive (Figs. 8 and 9), and the dependence on the breathing mode distortion is different depending on the reference magnetic order.

For the case of FM order, the next-nearest neighbor exchange interactions between LB nickel atoms gradually increase, while for the SB nickels they gradually decrease to zero; this is the same trend as the magnetic moments, see Fig. 4. In contrast, for the T-AFM order, the SB magnetic moments are suppressed and thus the magnetic interactions between LB nickel atoms jump abruptly to a large value with $R_1^+ > 0$. Further increasing R_1^+ results in a small reduction in the magnitude of the exchange coupling. The behavior in Fig. 8(a) hints at a strong coupling between R_1^+ distortion and T-AFM order. Overall, exchange couplings between LB nickel sites at both reference magnetic configurations have the same order of magnitude. The values of J_4 and J_7 at $R_1^+ = 0$ are about an order of magnitude smaller than J_1/J_5, and

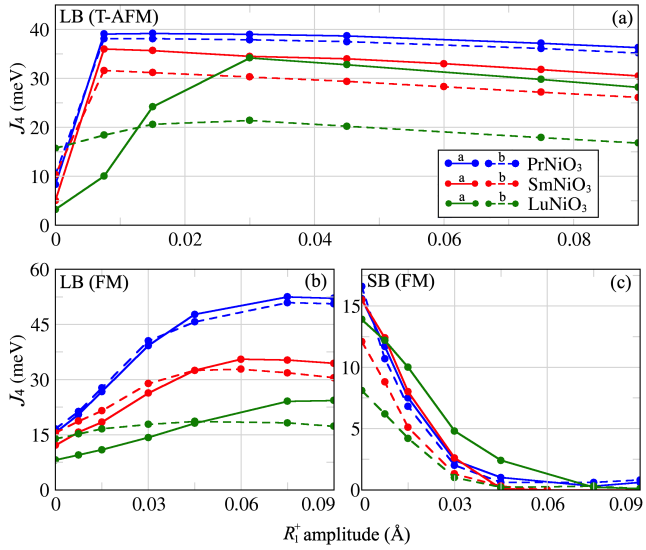

FIG. 8. Next nearest neighbor $J_4^{a/b}$ magnetic interactions between nickel atoms in $\mathcal{R}$NiO$_3$ as a function of breathing mode distortion R_1^+ and reference magnetic order: (a) interactions between LB atoms in T-AFM order, while (b) and (c) correspond to interactions between LB and SB in FM order, respectively. Notation of magnetic couplings corresponds to Fig. 6.

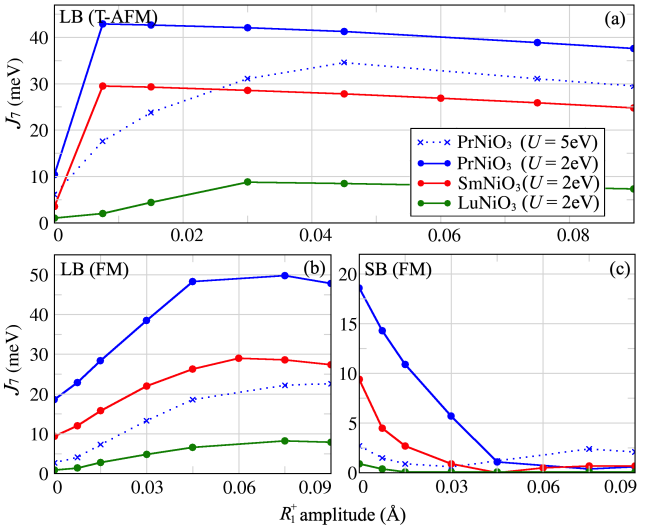

FIG. 9. Next nearest neighbor J_7 magnetic interactions between nickel atoms in $\mathcal{R}$NiO$_3$ as a function of breathing mode distortion R_1^+ and reference magnetic order: (a) interactions between LB atoms in T-AFM order, while (b) and (c) correspond to interactions between LB and SB in FM order, respectively. Additional dotted curve for PrNiO$_3$ denoted by crosses represents results obtained with U = 5 eV. Notation of magnetic couplings corresponds to Fig. 6.

thus the T-AFM magnetic configuration is fragile. Since the main mechanism of the next nearest interactions is superexchange, all these couplings weaken for a larger U value, which is shown for J_7 of PrNiO$_3$ in Fig. 9.

TABLE I. Orbital resolved exchange couplings (in meV) for PrNiO$_3$, SmNiO$_3$ and LuNiO$_3$, calculated (U=2 eV) using experimental breathing mode amplitudes R_1^+ for PrNiO$_3$ and LuNiO$_3$, and the theoretical one for SmNiO$_3$. Notation of magnetic couplings corresponds to Fig. 6. Note, that the "total" exchange coupling includes the contribution from the t_{2g} states (not shown).

		PrNiO$_3$	SmNiO$_3$	LuNiO$_3$
R_1^+		0.045 Å[50]	0.060 Å[33]	0.075 Å[51]
J_{1a}/J_{1b}	d_{z^2}	-26.9/-26.5	-25.9/-21.4	-30.3/-17.3
	$d_{x^2-y^2}$	-78.9/-78.7	-65.7/ -60.8	-54.9/-40.6
	total	-103.9/-102.6	-89.4/-80.2	-83.6/-59.8
J_5	d_{z^2}	-96.5	-83.0	-64.4
	$d_{x^2-y^2}$	-1.2	-0.8	-0.6
	total	-96.7	-81.4	-60.7
J_{4a}/J_{4b}	d_{z^2}	10.3/10.4	10.1/8.7	11.4/6.3
	$d_{x^2-y^2}$	30.1/29.6	23.6/20.6	17.8/10.6
	total	38.7/37.5	33.0/28.3	29.8/17.9
J_7	d_{z^2}	44.2	29.8	8.8
	$d_{x^2-y^2}$	0.0	0.0	0.0
	total	41.3	26.9	7.7
J_2	d_{z^2}	3.5	4.1	5.4
	$d_{x^2-y^2}$	0.2	3.9	5.0
	total	3.5	7.5	10.0
J_3	d_{z^2}	2.1	2.2	5.1
	$d_{x^2-y^2}$	7.6	9.4	10.2
	total	9.9	11.6	16.0
J_{6a}/J_{6b}	d_{z^2}	6.8/4.2	4.5/5.3	2.7/7.0
	$d_{x^2-y^2}$	5.0/3.2	3.2/2.4	3.3/1.5
	total	12.1/7.6	7.8/7.7	6.2/8.5

3. *Summary and remaining exchange couplings*

The values for the exchange interactions discussed above, calculated at the experimental R_1^+ amplitudes[50,51] (except for SmNiO$_3$ where we use the theoretical value from Ref. 33), are given in Table I. Also included are the remaining couplings shown in Fig. 6: J_2, J_3, and J_6; we see that these couplings are small compared to J_1/J_5 and J_4/J_7. This is because of the geometry of the active e_g orbitals, which overlap via oxygen atoms along the Cartesian axes (Fig. 6). Our orbital resolved analysis of the exchange interactions (Eq. 2) demonstrates that the main contribution to the in-plane J_1 and J_4 couplings comes from $d_{x^2-y^2}$ and d_{z^2} orbitals, while out-of-plane J_5 and J_7 couplings originate from d_{z^2} states (See Table I). The overlap of $d_{x^2-y^2}$ and d_{z^2} orbitals is sensitive to the Ni – O – Ni angle, which is influenced by the octahedral rotations and breathing distortions. Overall, this

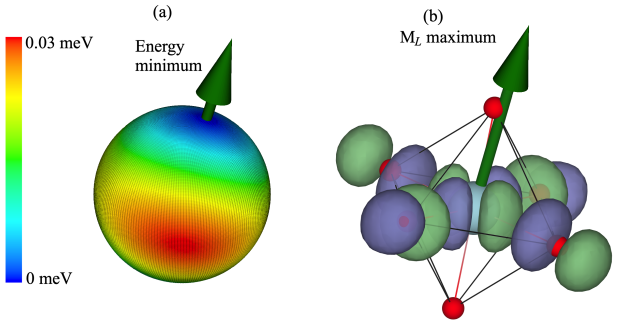

FIG. 10. Anisotropic energy map for $PrNiO_3$ system. The arrow indicates the energy minimum, which is close to the direction of apical oxygen position of MoO_6 octahedra, depicted in (b) together with Wannier function of $x^2 - y^2$ symmetry, the valence electron in which state induces orbital magnetic moment.

leads to a significant increase of the exchange couplings going from Lu to Pr, i.e., when octahedral rotations are reduced.

C. Anisotropy and non-collinear order

To shed light on the long-standing question of collinear versus noncollinear (NCL) order in rare-earth nickelates (Fig. 2), we also performed an analysis of the magnetic anisotropy and NCL magnetic arrangements within DFT+U calculations taking spin-orbit coupling (SOC) into account. In the case of the proposed[25,26,58] NCL magnetic order, nearest-neighbor magnetic moments are orthogonal to each other [Fig. 2(b)]. Since $\mathbf{m}_{\rm LB} \cdot \mathbf{m}_{\rm SB} = 0$, the contributions of the strong isotropic ferromagnetic J_1/J_5 couplings are eliminated, and magnetic frustration between FM nearest-neighbors and AFM next-nearest-neighbors couplings does not occur.

We perform calculations including SOC on the *Pbnm* crystal structure of $PrNiO_3$, $SmNiO_3$, and $LuNiO_3$ with breathing mode amplitudes given in Table I. We find that the SB moments for all three materials vanish in these calculations, analogously to the collinear calculations in Fig. 4. The LB moment is always nonzero and equals 1.19 μ_B, 1.24 μ_B and 1.28 μ_B for $\mathcal{R}$ = Pr, Sm and Lu, respectively. Thus, the NCL configuration we find is equivalent to the collinear T-AFM order, with the LB magnetic moments free to align along the direction which minimizes the anisotropy energy in the systems; we can find this direction by calculating the anisotropic energy map[59].

In Fig. 10(a), we show the interpolated anisotropic energy map for $PrNiO_3$. To generate this plot, DFT+U+SOC calculations were performed using magnetic moments constrained along various (uniformly distributed) directions, but keeping their mutual orientation consistent with T-AFM order. We find an easy axis along a direction close to the position of the apical oxygen atom in the NiO_6 octahedra [green arrow in Fig. 10(a)], which we label as the z-axis. The anisotropy in the energy is very small (~ 0.03 meV), which is expected for $3d$ systems with weak SOC[44,45]. According to conventional theories of magnetocrystalline anisotropy (i.e., Brunos model[60,61]), the orbital moment is maximized when the magnetization points along the easy axis. This is true for $\mathcal{R}NiO_3$ systems, showing the maximum value of orbital moment $M_L = 0.13$ μ_B aligned with spin magnetic moment 1.19 μ_B along the direction of the easy axis.

The orbital moment is induced by e_g electrons, which can be seen on the level of density matrix $\hat{N}$:

$$M_L = \mathrm{Tr}(\hat{N} \cdot \hat{L}_z).$$

In particular, the valence electron occupying the d_{z^2} will not produce any orbital moment ($\hat{L}_z d_{z^2} = 0$). On the other hand, due to a non-zero $\langle d_{xy}|\hat{L}_z|d_{x^2-y^2}\rangle = 2i$, and the fact that the calculated density matrix contains imaginary components between d_{xy} and $d_{x^2-y^2}$ states, an orbital moment is induced along the direction of the apical oxygen in the NiO_6 octahedra (z-axis) by the electron in the $d_{x^2-y^2}$ state. This leads to the formation of the easy axis anisotropy found by in our DFT+U+SOC calculations (Fig. 10).

IV. DISCUSSION

The goal of the calculations in Sec. III was to elucidate two key issues regarding the magnetic structure in RE nickelates: (a) why DFT+U favors a FM solution, while an AFM structure with propagation vector $\mathbf{q} = (\frac{1}{4}, \frac{1}{4}, \frac{1}{4})$ is observed experimentally; and (b) what is the relation between the T-AFM magnetic structure determined from neutron diffraction data, and the NCL magnetic structure determined from RIXS. Furthermore, an additional aim was to understand the mechanisms driving the trends in magnetic-phase stability across the series.

We find that the key physical mechanism at play in these systems is the competition between strong nearest-neighbor ferromagnetic J_1/J_5 and the much weaker next-nearest-neighbor antiferromagnetic J_4/J_7. This competition causes magnetic frustration, and works to destabilize the long-range magnetic order. As discussed before, the R_1^+ distortion will result in different magnetic moments on the LB and SB Ni atoms, with the SB magnetic moment suppressed (Fig. 4). Therefore, the energy gain from forming ferromagnetic order will be directly proportional to the SB moment. Hence, the reason why DFT+U favors FM order[1,2] is the overestimation of short bond magnetic moments, leading to a larger contribution of nearest-neighbor FM couplings, which makes the FM solution energetically favorable. For a sufficiently small SB moment the FM J_1 and J_5 interactions are suppressed, and the next-nearest neighbor AFM couplings J_4 and J_7 will dominate; the result is the collinear T-AFM order proposed from neutron diffraction experi-

ments[11,21–23] (Fig. 2). As we saw in Fig. 4, the SB moments go to zero rapidly with increasing R_1^+ amplitude in the T-AFM ordering to avoid the energy penalty associated with a finite FM J_1/J_5 coupling. The reason for the discrepancy between theory and experiment, could be due to an overestimation of exchange splitting in DFT+U, or problems in the refinement of experimental data. For a future analysis it would be of high interest to incorporate self-energy corrections to the Green's function exchange coupling analysis from higher order theory, i.e, GW or dynamical mean-field theory, to rule out problems due to dynamic correlation effects[62].

Another approach to avoiding frustration is the proposed magnetic structure from RIXS experiments[25,26]. The NCL ordering where the nearest-neighbor moments point in orthogonal directions, has no energy penalty for AFM versus FM ordering, and thus does not require the strong reduction of the SB magnetic moment needed for stabilization of collinear antiferromagnetic order. However, as discussed in Sec. III C, we cannot stabilize this ordering in our calculations, as the SB moment vanishes at the experimental R_1^+ amplitude, even if a SOC is included (thus a NCL order is allowed). The origin of the SB magnetic suppression can be related to the symmetry of the magnetic configurations. The SB magnetic moment is surrounded by four LB nickel atoms within the ab plane (Fig. 2), and in the case of FM order, this will enhance the local magnetic polarization on the SB nickel atom, increasing its magnetic moment. Since in T-AFM order (and also the NCL order) half of the neighboring LB moments are aligned parallel, and the other half antiparallel, the SB moment will be reduced. The valence electron in the magnetically active $d_{x^2-y^2}$ states induces an orbital moment $M_L \simeq 0.13\ \mu_B$ pointed at the apical oxygen position of the NiO_6 octahedra. This leads to the formation of easy-axis anisotropy, giving a preferable direction for LB magnetic moments alignment.

The analysis above is for the experimental R_1^+ amplitudes (theoretical for $SmNiO_3$); however, we see that these results are robust over a wide range of R_1^+ amplitudes. Increasing the breathing distortion reduces FM nearest neighbor J_1/ J_5 interactions and magnetic moments of SB nickel atoms, thus it can strengthen the long range T-AFM ordering in these systems. This explains the observation[1] in DFT+U that R_1^+ (FM) $<$ R_1^+(T-AFM).

RIXS experiments for thin film $NdNiO_3$ samples revealed that the in ab-plane next-nearest-neighbor interaction J_4 is stronger than the nearest neighbor J_2 coupling $J_4 \simeq 2J_2$[26]. In our calculations we also observe $J_4 \gg J_2$ (Table I). Furthermore, we found strong spacial anisotropy depending on RE element, which splits interactions in the ab plane into two groups: nearest-neighbor J_{1a}/J_{1b}, next-nearest-neighbor J_2/J_3 and next-next-nearest neighbor J_{4a}/J_{4b} (Fig. 6). Moreover, we see a strong difference between ab plane (J_1/J_4) and out-of-plane c-direction (J_5/J_7) exchange couplings depending on RE element.

Finally, the results provide a clear picture of the trends of the magnetic order across the nickelate series. While the larger octahedral distortions (R_4^+, M_3^+) present for smaller RE ions make the system more susceptible to the insulating breathing-mode-distorted state[19,32], we find that they also reduce the exchange couplings, making the formation of the magnetically ordered state less favorable. Importantly, we find that this observation is not specific to the experimental R_1^+ amplitude, but holds for all $R_1^+ > 0$ (see Figs. 7, 8, and 9). These findings explain the experimentally-observed reduction in stability of magnetic order in the low temperature insulating phase across the series towards $LuNiO_3$[3,22].

V. CONCLUSIONS

Based on DFT+U calculations, Wannier orbitals and Green's function techniques, we constructed microscopic magnetic models for selected RE nickelate systems ($PrNiO_3$, $SmNiO_3$, and $LuNiO_3$) and studied the evolution of their parameters under the R_1^+ breathing mode distortion and reference magnetic configuration. Our theoretical results help to clarify several issues related to these systems, and provide insights into the mechanisms driving the complex magnetic state of RE nickelates. The Wannier function based analysis demonstrates that the magnetic moments reside on nickel atoms, and are induced by active Ni e_g states. The main exchange interactions are strong ferromagnetic interactions arising from double exchange between the nearest neighbor nickels, and somewhat weaker antiferromagnetic interactions between the next-nearest neighbor nickels induced by a kinetic superexchange mechanism. The competition between these, together with the R_1^+ distortion, determines the magnetic order.

The stronger nearest-neighbor interactions are the reason that DFT+U calculations find the ferromagnetic state to be lowest in energy. The stabilization of collinear T-AFM order, which is compatible with the experimental symmetry, is possible due to suppression of the SB magnetic moments with the onset of the breathing mode distortion, eliminating the contribution of the ferromagnetic interactions. We find that even if spin-orbit coupling is included and a non-collinear ordering is allowed, the SB Ni moments are still suppressed, and T-AFM order is restored with an easy axis magnetization pointed towards the apical oxygen. Thus our work determines the reason for the general disagreement between the DFT-U predicted magnetic order (FM) and experiment (AFM), provides a clear explanation how the $\mathbf{q} = (\frac{1}{4}, \frac{1}{4}, \frac{1}{4})$ magnetic order emerges in rare-earth nickelates, and demonstrates how these trends evolve across the series.

ACKNOWLEDGMENTS

D.I.B. is grateful to S. A. Nikolaev (Tokyo Institute of Technology) for helpful discussions. The calculations have been performed using the facilities of the Flatiron Institute. The Flatiron Institute is a division of the Simons Foundation. C.E.D. acknowledge support from the National Science Foundation under Grant No. DMR-1918455.

* ahampel@flatironinstitute.org

[1] A. Hampel and C. Ederer, Phys. Rev. B **96**, 165130 (2017).
[2] J. Varignon, M. N. Grisolia, J. Íñiguez, A. Barthélémy, and M. Bibes, npj Quantum Materials **2**, 21 (2017).
[3] S. Catalano, M. Gibert, J. Fowlie, J. Íñiguez, J.-M. Triscone, and J. Kreisel, Rep. Prog. Phys. **81**, 046501 (2018).
[4] Y. Lu, Z. Zhong, M. W. Haverkort, and P. Hansmann, Phys. Rev. B **95**, 195117 (2017).
[5] X. Obradors, L. M. Paulius, M. B. Maple, J. B. Torrance, A. I. Nazzal, J. Fontcuberta, and X. Granados, Phys. Rev. B **47**, 12353 (1993).
[6] S. Catalano, M. Gibert, V. Bisogni, O. E. Peil, F. He, R. Sutarto, M. Viret, P. Zubko, R. Scherwitzl, A. Georges, G. A. Sawatzky, T. Schmitt, and J.-M. Triscone, APL Materials **2**, 116110 (2014).
[7] A. V. Boris, Y. Matiks, E. Benckiser, A. Frano, P. Popovich, V. Hinkov, P. Wochner, M. Castro-Colin, E. Detemple, V. K. Malik, C. Bernhard, T. Prokscha, A. Suter, Z. Salman, E. Morenzoni, G. Cristiani, H.-U. Habermeier, and B. Keimer, Science **332**, 937 (2011).
[8] C. Y, B. L., Y. Sun, H. Yang, and X. Zhang, Electrochimica Acta **174**, 41 (2015).
[9] J. Shi, Y. Zhou, and S. Ramanathan, Nature Communications **5**, 4860 (2014).
[10] S.-W. Cheong and M. Mostovoy, Nature Materials **6**, 13 (2007).
[11] J. A. Alonso, J. L. García-Muñoz, M. T. Fernández-Díaz, M. A. G. Aranda, M. J. Martínez-Lope, and M. T. Casais, Phys. Rev. Lett. **82**, 3871 (1999).
[12] I. I. Mazin, D. I. Khomskii, R. Lengsdorf, J. A. Alonso, W. G. Marshall, R. M. Ibberson, A. Podlesnyak, M. J. Martínez-Lope, and M. M. Abd-Elmeguid, Phys. Rev. Lett. **98**, 176406 (2007).
[13] S. Johnston, A. Mukherjee, I. Elfimov, M. Berciu, and G. A. Sawatzky, Phys. Rev. Lett. **112**, 106404 (2014).
[14] R. J. Green, M. W. Haverkort, and G. A. Sawatzky, Phys. Rev. B **94**, 195127 (2016).
[15] H. Park, A. J. Millis, and C. A. Marianetti, Phys. Rev. Lett. **109**, 156402 (2012).
[16] B. Lau and A. J. Millis, Phys. Rev. Lett. **110**, 126404 (2013).
[17] A. Subedi, O. E. Peil, and A. Georges, Phys. Rev. B **91**, 075128 (2015).
[18] K. Haule and L. Pascut, G, Scientific Reports **7**, 10375 (2017).
[19] O. E. Peil, A. Hampel, C. Ederer, and A. Georges, Phys. Rev. B **99**, 245127 (2019).
[20] G. Kresse and D. Joubert, Phys. Rev. B **59**, 1758 (1999).
[21] J. L. García-Muñoz, J. Rodríguez-Carvajal, and P. Lacorre, Phys. Rev. B **50**, 978 (1994).
[22] D. J. Gawryluk, Y. M. Klein, T. Shang, D. Sheptyakov, L. Keller, N. Casati, P. Lacorre, M. T. Fernández-Díaz, J. Rodríguez-Carvajal, and M. Medarde, Phys. Rev. B **100**, 205137 (2019).
[23] A. Muñoz, J. A. Alonso, M. J. Martínez-Lope, and M. T. Fernández-Díaz, J. Solid State Chem. **182**, 1982 (2009).
[24] M. T. Fernández-Díaz, J. A. Alonso, M. J. Martínez-Lope, M. T. Casais, and J. L. García-Muñoz, Phys. Rev. B **64**, 144417 (2001).
[25] V. Scagnoli, U. Staub, A. M. Mulders, M. Janousch, G. I. Meijer, G. Hammerl, J. M. Tonnerre, and N. Stojic, Phys. Rev. B **73**, 100409 (2006).
[26] Y. Lu, D. Betto, K. Fürsich, H. Suzuki, H.-H. Kim, G. Cristiani, G. Logvenov, N. B. Brookes, E. Benckiser, M. W. Haverkort, G. Khaliullin, M. Le Tacon, M. Minola, and B. Keimer, Phys. Rev. X **8**, 031014 (2018).
[27] R. J. Hepting, M.and Green, Z. Zhong, M. Bluschke, Y. E. Suyolcu, S. Macke, A. Frano, S. Catalano, M. Gibert, R. Sutarto, F. He, G. Cristiani, Y. Logvenov, G.and Wang, P. A. van Aken, P. Hansmann, M. Le Tacon, J.-M. Triscone, G. A. Sawatzky, and E. Keimer, B.and Benckiser, Nature Physics **14**, 1097 (2018).
[28] F. Y. Bruno, K. Z. Rushchanskii, S. Valencia, Y. Dumont, C. Carrétéro, E. Jacquet, R. Abrudan, S. Blügel, M. Ležaić, M. Bibes, and A. Barthélémy, Phys. Rev. B **88**, 195108 (2013).
[29] G. Giovannetti, S. Kumar, D. Khomskii, S. Picozzi, and J. van den Brink, Phys. Rev. Lett. **103**, 156401 (2009).
[30] S. Prosandeev, L. Bellaiche, and J. Íñiguez, Physical Review B **85**, 214431 (2012).
[31] Z. He and A. J. Millis, Physical Review B **91**, 195138 (2015).
[32] A. Mercy, J. Bieder, J. Íñiguez, and P. Ghosez, Nat. Commun. **8**, 1677 (2017).
[33] A. Hampel, P. Liu, C. Franchini, and C. Ederer, npj Quantum Materials **4**, 5 (2019).
[34] A. Liechtenstein, M. Katsnelson, V. Antropov, and V. Gubanov, Journal of Magnetism and Magnetic Materials **67**, 65 (1987).
[35] V. V. Mazurenko and V. I. Anisimov, Phys. Rev. B **71**, 184434 (2005).
[36] K. Momma and F. Izumi, J. Appl. Crystallogr. **44**, 1272 (2011).
[37] For simplicity, we use spin quantum number $S = \frac{1}{2}$ in Eq. (2) during the whole range of breathing distortions. It was revealed that very large breathing distortion amplitudes are needed to achieve spins 0 and 1 for SB and LB magnetic moments[13,14], which is much higher than our considered cases.
[38] J. Perdew, K. Burke, and M. Ernzerhof, Phys. Rev. Lett. **77**, 3865 (1996).
[39] P. E. Blöchl, Phys. Rev. B **50**, 17953 (1994).
[40] G. Kresse and J. Furthmüller, Computa. Mater. Sci. **6**, 15 (1996).
[41] G. Kresse and J. Furthmüller, Phys. Rev. B **54**, 11169 (1996).

[42] V. I. Anisimov, J. Zaanen, and O. K. Andersen, Phys. Rev. B **44**, 943 (1991).

[43] A. I. Liechtenstein, V. I. Anisimov, and J. Zaanen, Phys. Rev. B **52**, R5467 (1995).

[44] D. I. Badrtdinov, O. S. Volkova, A. A. Tsirlin, I. V. Solovyev, A. N. Vasiliev, and V. V. Mazurenko, Phys. Rev. B **94**, 054435 (2016).

[45] D. I. Badrtdinov, V. V. Mazurenko, and A. A. Tsirlin, Phys. Rev. B **100**, 214401 (2019).

[46] N. Marzari and D. Vanderbilt, Phys. Rev. B **56**, 12847 (1997).

[47] G. Pizzi, V. Vitale, R. Arita, S. Blügel, F. Freimuth, G. Géranton, M. Gibertini, D. Gresch, C. Johnson, T. Koretsune, J. Ibañez-Azpiroz, H. Lee, J.-M. Lihm, D. Marchand, A. Marrazzo, Y. Mokrousov, J. I. Mustafa, Y. Nohara, Y. Nomura, L. Paulatto, S. Poncé, T. Ponweiser, J. Qiao, F. Thöle, S. S. Tsirkin, M. Wierzbowska, N. Marzari, D. Vanderbilt, I. Souza, A. A. Mostofi, and J. R. Yates, Journal of Physics: Condensed Matter **32**, 165902 (2020).

[48] J. M. Perez-Mato, D. Orobengoa, and M. I. Aroyo, Acta Crystallographica Section A **66**, 558 (2010).

[49] P. V. Balachandran and J. M. Rondinelli, Physical Review B **88**, 054101 (2013).

[50] M. Medarde, M. T. Fernández-Díaz, and P. Lacorre, Phys. Rev. B **78**, 212101 (2008).

[51] J. A. Alonso, M. J. Martínez-Lope, M. T. Casais, J. L. García-Muñoz, M. T. Fernández-Díaz, and M. A. G. Aranda, Phys. Rev. B **64**, 094102 (2001).

[52] J. L. García-Muñoz, J. Rodríguez-Carvajal, and P. Lacorre, Europhys. Lett. **20**, 241 (1992).

[53] J. L. García-Muñoz, P. Lacorre, and R. Cywinski, Phys. Rev. B **51**, 15197 (1995).

[54] D. I. Badrtdinov, S. A. Nikolaev, A. N. Rudenko, M. I. Katsnelson, and V. V. Mazurenko, Phys. Rev. B **98**, 184425 (2018).

[55] X. Zhu, A. Edström, and C. Ederer, Phys. Rev. B **101**, 064401 (2020).

[56] C. Zener, Phys. Rev. **82**, 403 (1951).

[57] S. Keshavarz, Y. O. Kvashnin, D. C. M. Rodrigues, M. Pereiro, I. Di Marco, C. Autieri, L. Nordström, I. V. Solovyev, B. Sanyal, and O. Eriksson, Phys. Rev. B **95**, 115120 (2017).

[58] M. Szwaja and F. Calvayrac, Journal of Physics: Conference Series **289**, 012002 (2011).

[59] A. H. Abdeldaim, D. I. Badrtdinov, A. S. Gibbs, P. Manuel, H. C. Walker, M. D. Le, C. H. Wu, D. Wardecki, S.-G. Eriksson, Y. Kvashnin, A. A. Tsirlin, and G. J. Nilsen, Phys. Rev. B **100**, 214427 (2019).

[60] P. Bruno, Phys. Rev. B **39**, 865 (1989).

[61] *Magnetism. From fundamentals to nanoscale dynamics* (Springer, Berlin Heidelberg, 2006).

[62] Y. O. Kvashnin, O. Grånäs, I. Di Marco, M. I. Katsnelson, A. I. Lichtenstein, and O. Eriksson, Phys. Rev. B **91**, 125133 (2015).